Science Advances
AAAS

Supplementary Materials for

Visible and infrared dual-band imaging via Ge/MoS_2 van der Waals heterostructure

Aujin Hwang, Minseong Park, Youngseo Park, Yeongseok Shim, Sukhyeong Youn, Chan-Ho Lee, Han Beom Jeong, Hu Young Jeong, Jiwon Chang, Kyusang Lee*, Geonwook Yoo*, Junseok Heo*

*Corresponding author. Email: kl6ut@virginia.edu (K.L.); gwyoo@ssu.ac.kr (G.Y.); jsheo@ajou.ac.kr (J.H.)

Published 15 December 2021, *Sci. Adv.* **7**, eabj2521 (2021)
DOI: 10.1126/sciadv.abj2521

This PDF file includes:

Supplementary Text
Figs. S1 to S18
Table S1
References

Supplementary Text

Density Functional Theory (DFT) Simulation

Band structures, local density of states (LDOS) and geometry optimization calculations are performed with DFT implemented in QuantumATK software (Synopsys) (*30*, *31*). We employ generalized gradient approximation (GGA) and SG15 pseudopotentials to represent exchange–correlation potentials and pseudopotentials, respectively. For Ge, pseudopotential projector shift (pps) is adopted to predict the correct band gap. First, we calculate the band structures of bulk Ge and bulk MoS_2 to ensure that the calculations reproduce the experimentally measured band gap well. A k-point mesh of 9×9×9 and a mesh cut-off energy of 100 Hartree are used for bulk Ge while a k-point mesh of 10×10×3 and a mesh cut-off energy of 75 Hartree for bulk MoS_2. Geometry optimizations are performed until the residual force on each atom becomes less than 0.05 eV $Å^{-1}$. As shown from the band structures of bulk Ge and bulk MoS_2 in Figure S18, calculated band gap sizes of bulk Ge and bulk MoS_2 are close to the experimentally reported values. For the LDOS calculation, Ge/MoS_2 heterostructure is constructed by putting MoS_2 on top of the Ge (100) surface as shown in Figure S9. Unsaturated Ge adatom on the (100) surface are passivated by the hydrogen adatom to prevent the effect of dangling bonds. Semi-infinite Ge and MoS_2 are assumed on the left and right sides of the structure, respectively. In LDOS plots, brighter color corresponds to higher LDOS values. Therefore, we can estimate the CB and VB edges of Ge and MoS_2 at each location of the Ge/MoS_2 heterostructure.

Evidence of Trap-assisted Tunneling Current at Photoconductive Mode

We measured the band alignment based on our experimental XPS, UPS, and EELS results showing the type-II band alignment with accumulation at the heterojunction interface (see Fig. 1F) (*32–36*). Generally, the 2D MoS_2 allows for such type-II configuration (*8*), but since the electron affinity of MoS_2 is larger than that of Ge, our proposed MoS_2/Ge heterojunction exhibits the accumulated type-II at the MoS_2 interface. The band structure is the general bending configuration in other similar work function combinations. Based on the type-II structure, the n-type MoS_2 to be more n^+-doped at the interface. To clarify the difference between the n-doped (unintentionally doped) and n^+-doped MoS_2 heterojunctions, we added case-by-case band alignments and FN plots. Figure. S6A shows the type-II heterojunction for both n-doped and n^+-doped MoS_2 structures. The shown band alignment as based on our experimentally measured XPS, UPS, and EELS results. The n^+-doping distribution leads to less bending of the MoS_2 side and allows the expansion of the depletion region more toward to the Ge side. This directional expansion is more obvious under reverse bias; the n^+-doped MoS_2 heterojunction allows the Ge region to be bent further. As a result, the thicker tunneling barrier is formed, reducing the tunneling effect. The lower dark current is thus attributed only to the diffusion current from thermally generated carriers, similarly to normal pn diodes. In contrast, the tunneling barrier of the n-doped MoS_2 heterostructure exhibits a thin triangle shape (due to the expanded depletion region), and this additional tunneling current (as a FN tunneling mechanism) contributes to the high dark current.

According to the ref. (*37*), the direct and FN tunneling currents can be expressed by

$$I_{Direct} \propto V exp\left(-\frac{4\pi d\sqrt{2m^*\varphi}}{h}\right)$$

$$I_{FN} \propto V^2 exp\left(-\frac{8\pi d\sqrt{2m^*\varphi^3}}{3heV}\right)$$

where d, m^*, φ, h are the tunneling thickness, effective electron mass, tunneling barrier, and the Plank constant. To identify which tunneling current type is incorporated in our MoS_2/Ge heterojunction, ln(I/V^2) vs 1/V (FN plot) curve is plotted based on the experimental and I-V data.

As shown in Fig. S6B, when $1/V < 1$, the n-doped MoS_2/Ge structure exhibits a linear-decrease curve, increasing the FN tunneling effect in this region (*37*). On the other hand, the n^+-doped MoS_2/Ge structure exhibits a quasi-linear-increase curve, which is not attributed to the FN tunneling effect. Although the increasing linear curve might be due to the direct tunneling, as shown in Fig. S6C, the linear curve implies that the current mechanism is not based on the direct tunneling (since ln(I/V) should be constant in this plot according to the I_{Direct} equation above), but based on the thermally generated carriers. Therefore, based on these results, our MoS_2/Ge heterojunction allows for the selective VIS detection (not detecting infrared) capability at the photoconductive mode via the high tunneling current.

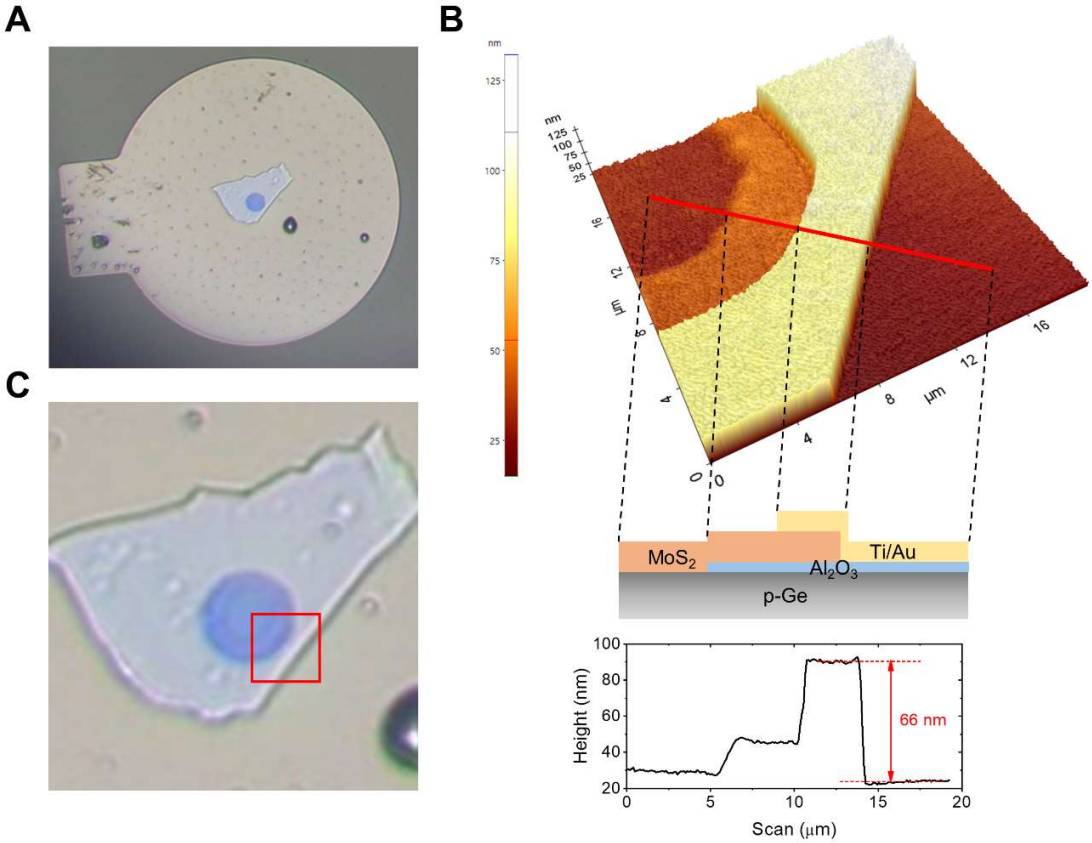

Fig. S1. Device height analysis. (**A**) Optical microscopy of the device. Scale-bar: 300 µm. (**B**) Atomic force microscopy map of the device with the corresponding cross-sectional device structure targeting on the (**C**) red box.

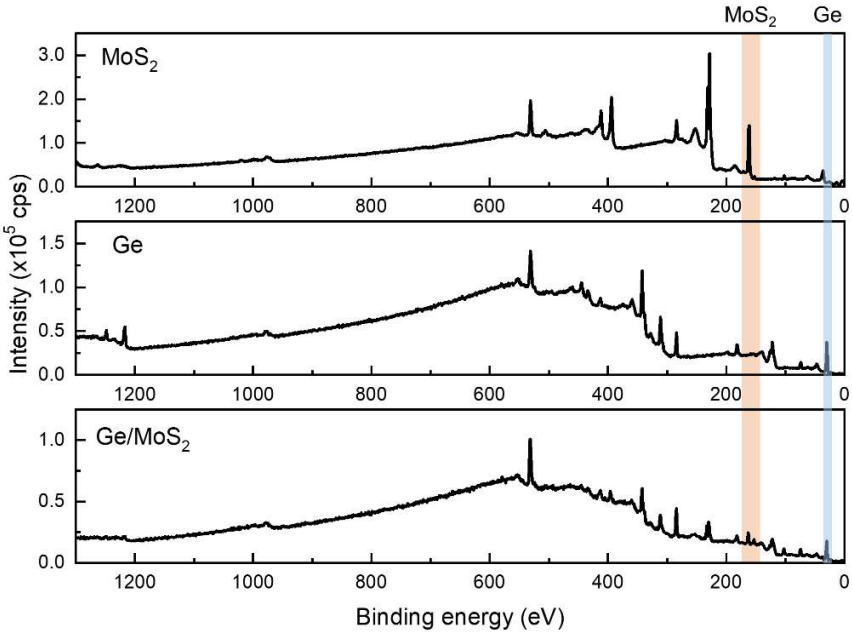

Fig. S2. X-ray photoelectron spectroscopy (XPS) survey spectra.

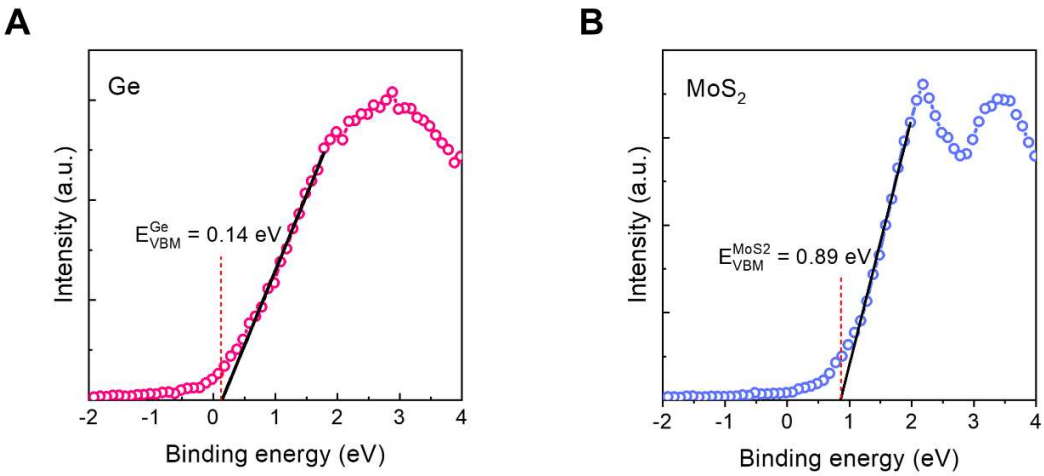

Fig. S3. Ultraviolet photoelectron spectroscopy (UPS) results. (**A**) Ge and (**B**) MoS_2.

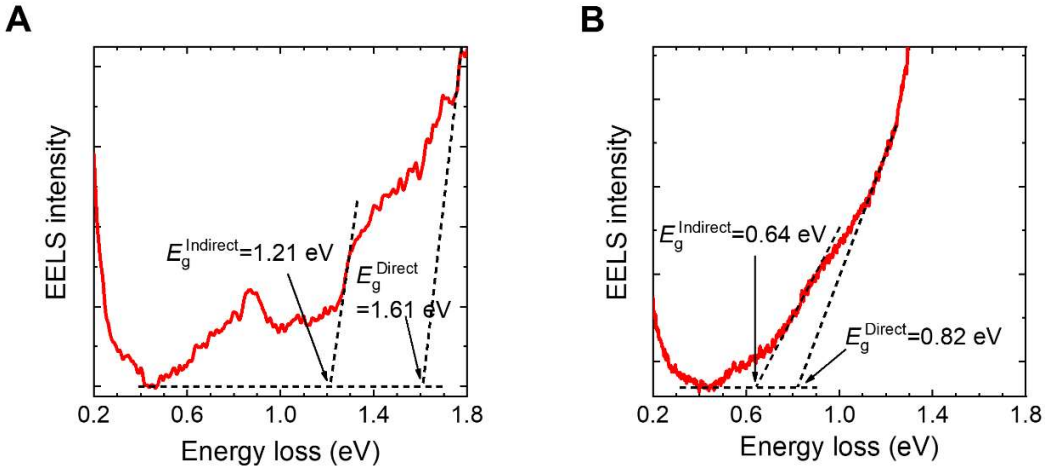

Fig. S4. Electron energy loss spectroscopy (EELS) results of MoS_2 and Ge. (**A**) EELS result of bulk MoS_2 and (**B**) EELS result of Ge. The corresponding indirect and direct bandgaps are 1.21 eV and 1.61 eV for Ge, respectively, and 0.64 eV and 0.82 eV for MoS_2, respectively.

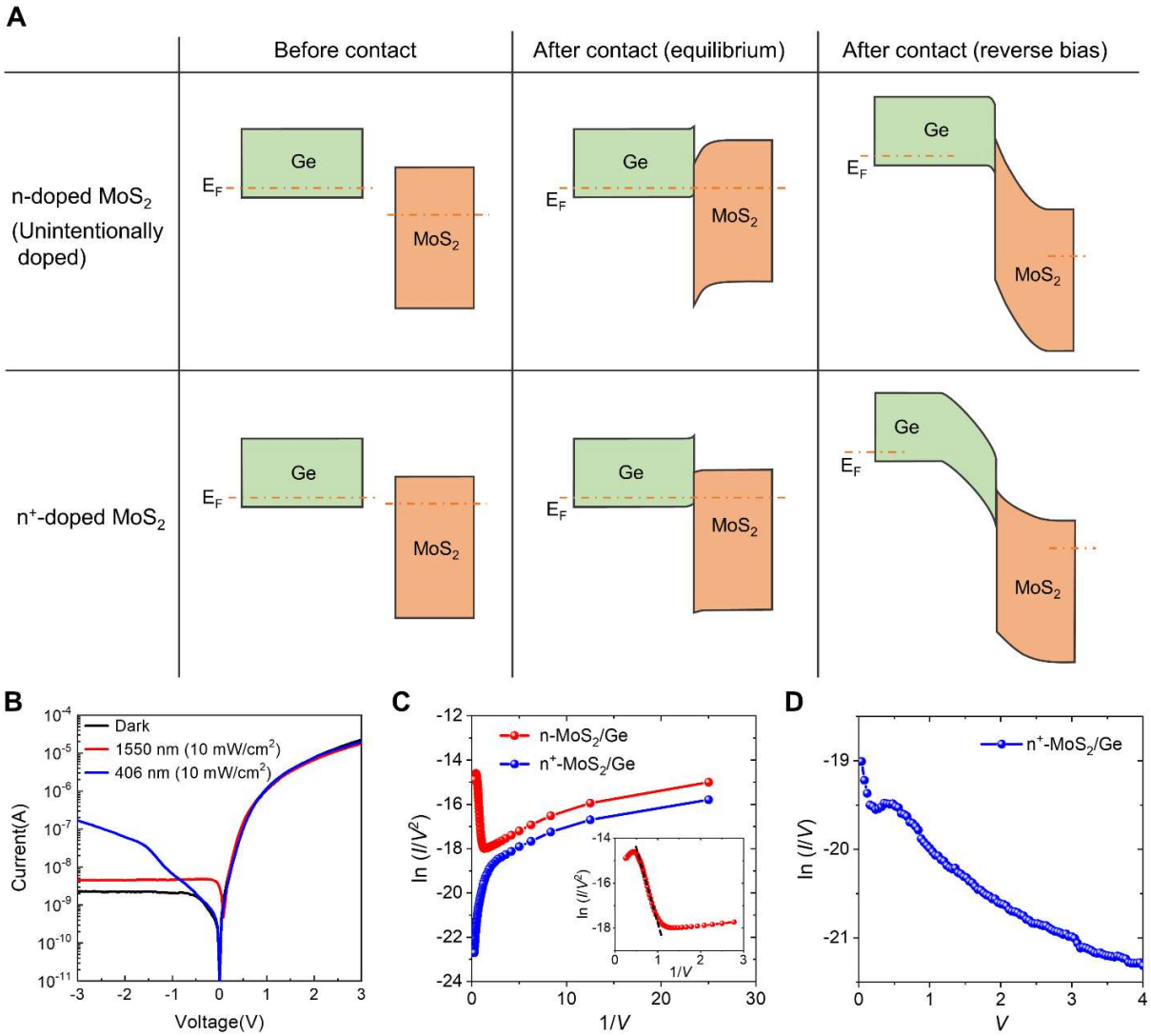

Fig. S5. Current characteristic comparison to n-doped (unintentionally doped)/n$^+$-doped MoS_2/Ge heterostructure. (**A**) Schematic band alignments for n-doped/n$^+$-doped MoS_2 at various states. (**B**) Current-voltage (*I–V*) characteristics of the Ge/n$^+$-MoS_2 photodetector in dark and at 466 and 1550 nm. The shift is due to the diffusion/drift transport of the photogenerated electrons and holes swept out from the depletion region, which is a general mechanism in photodetectors and solar cells. (**C**) Fowler-Nordheim (FN) plots. (**D**) ln(*I*/*V*) vs *V* plots.

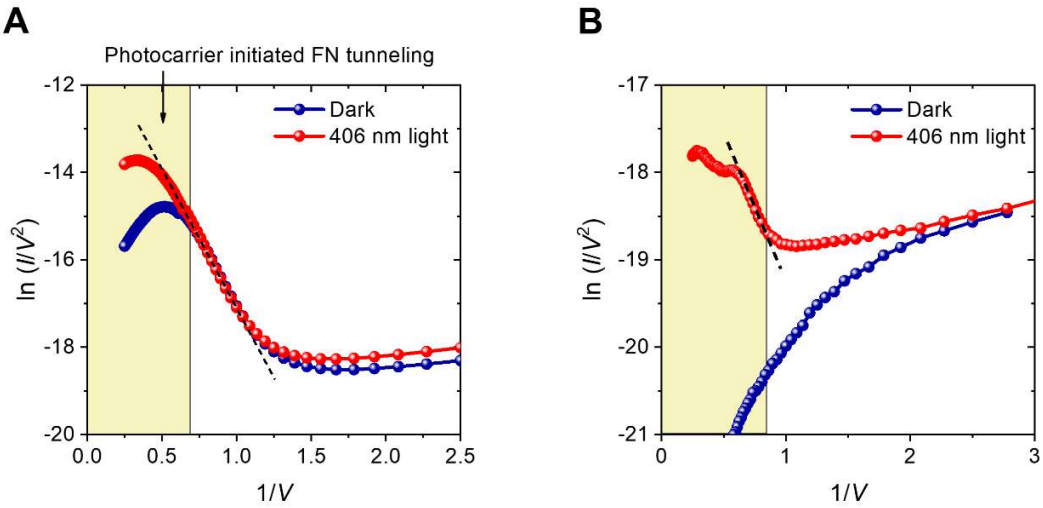

Fig. S6. Light/dark Fowler-Nordheim (FN) plots. FN plots for (**A**) n-doped (unintentionally doped) and (**B**) n^+-doped MoS_2/Ge heterojunction photodiodes.

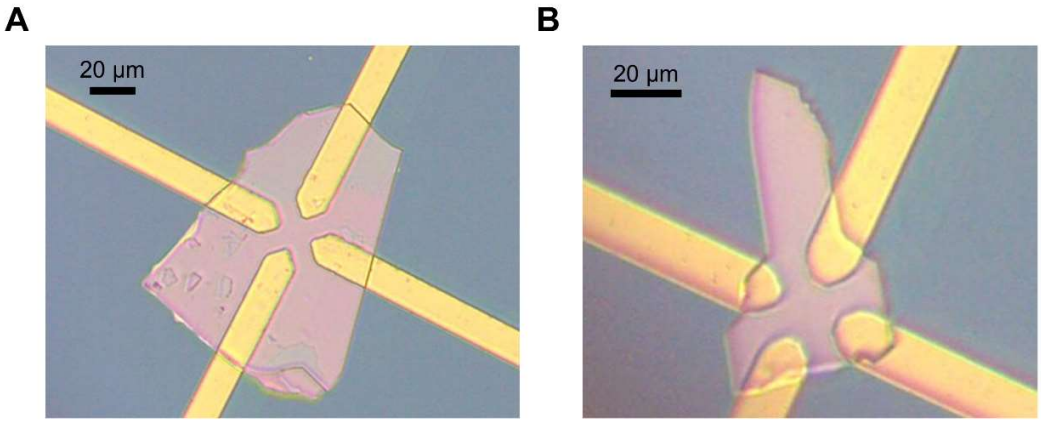

Fig. S7. Optical microscopy image of MoS_2. (**A**) n-doped (unintentionally doped) MoS_2. The measured surface carrier concentration (n_s), mobility, and doping concentration are 5.337×10^9 cm^{-2}, 188 $cm^2/V\cdot s$, and 7.624×10^{14} cm^{-3}, respectively. (**B**) n^+-doped MoS_2. The measured n_s, mobility, and doping concentration are 3.869×10^9 cm^{-2}, 23.69 $cm^2/V\cdot s$, and 5.528×10^{17} cm^{-3}, respectively.

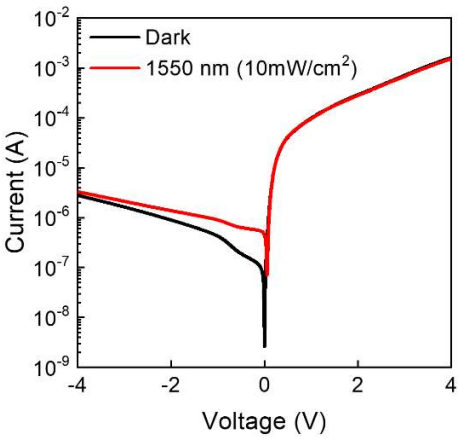

Fig. S8. Current-voltage (*I-V*) characteristics of pn-Ge.

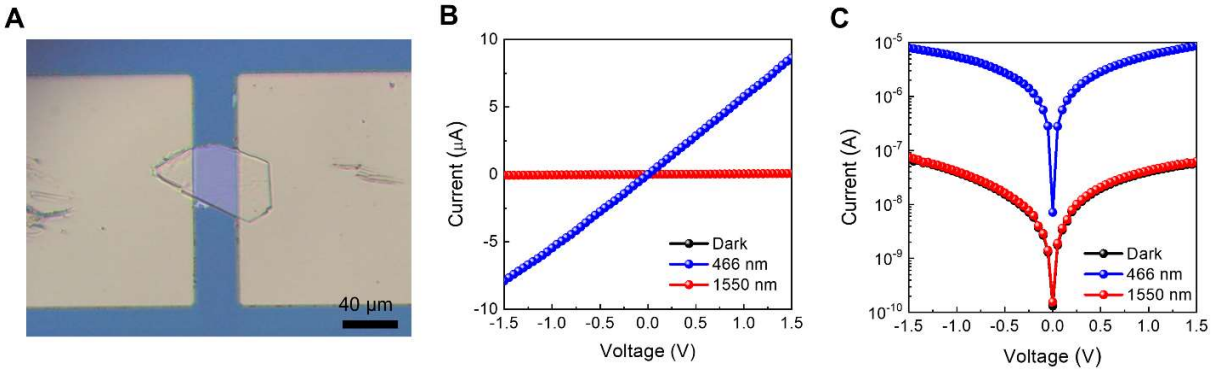

Fig. S9. MoS_2/Ti/Au Schottky diode. (**A**) Optical microscopy image of the diode including a MoS_2 flake. Current-voltage (*I-V*) characteristics of the diode under dark, 466 nm, and 1550 nm conditions in (**B**) linear scale and (**C**) logarithmic scale. The light intensity is 30 mW/cm^2.

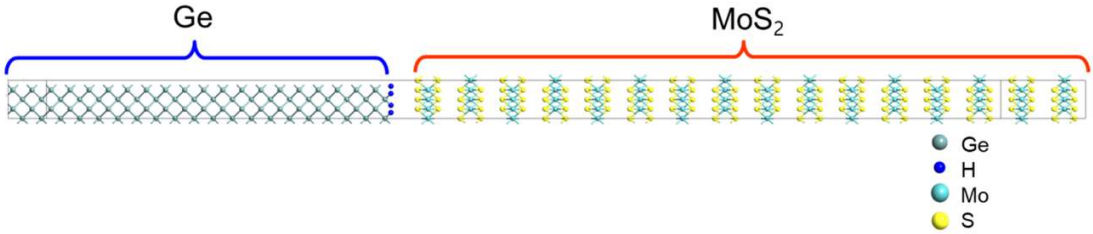

Fig. S10. Simulated Ge/MoS_2 heterostructure.

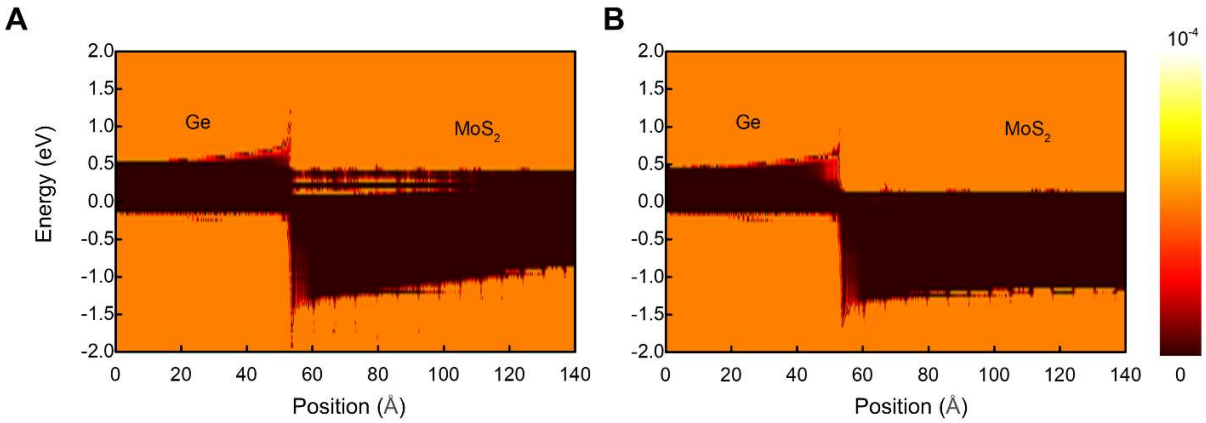

Fig. S11. Density functional theory (DFT) simulations. (**A**) Ge/MoS_2 heterostructure. (**B**) Heterostructure of Ge and n^+-doped MoS_2. Color map: local density of states [$Å^{-3}\cdot eV^{-1}$].

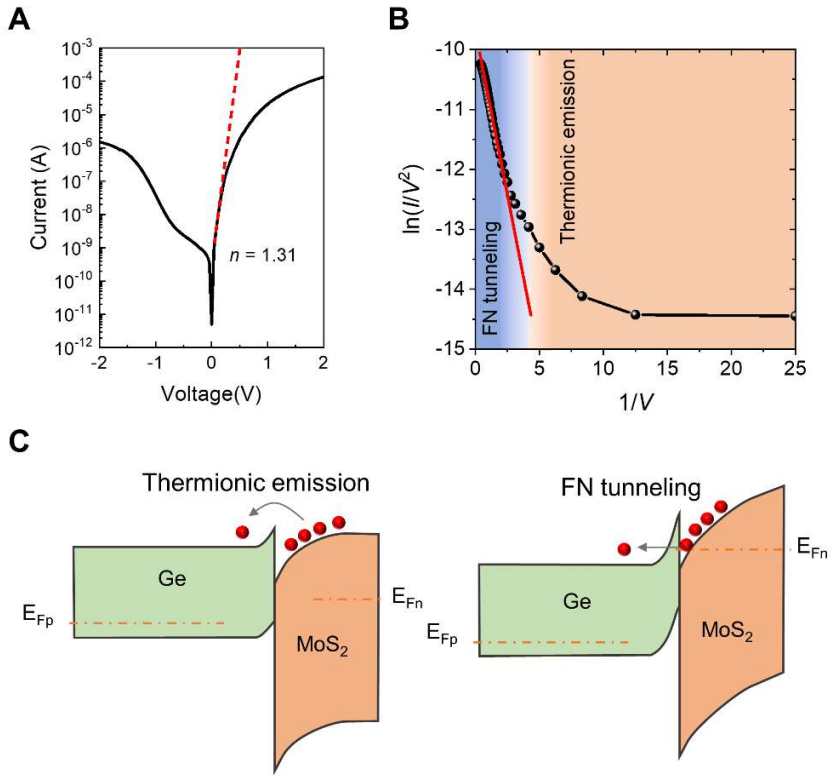

Fig. S12. Current transport characteristics. (**A**) Current-voltage (*I-V*) characteristic with ideality factors under dark condition. (**B**) Fowler-Nordheim (FN) plots. At $0 < 1/V < 2.27$ V, the plot shows a linear curve, implying the FN tunneling dominance in this voltage region. (**C**) Schematic band diagrams. At small forward bias, a thermionic emission of electrons in the MoS_2 over the conduction band offset mostly contribute to a forward current. As a forward bias increases, the barrier becomes a thinner, allowing the FN tunneling of electrons.

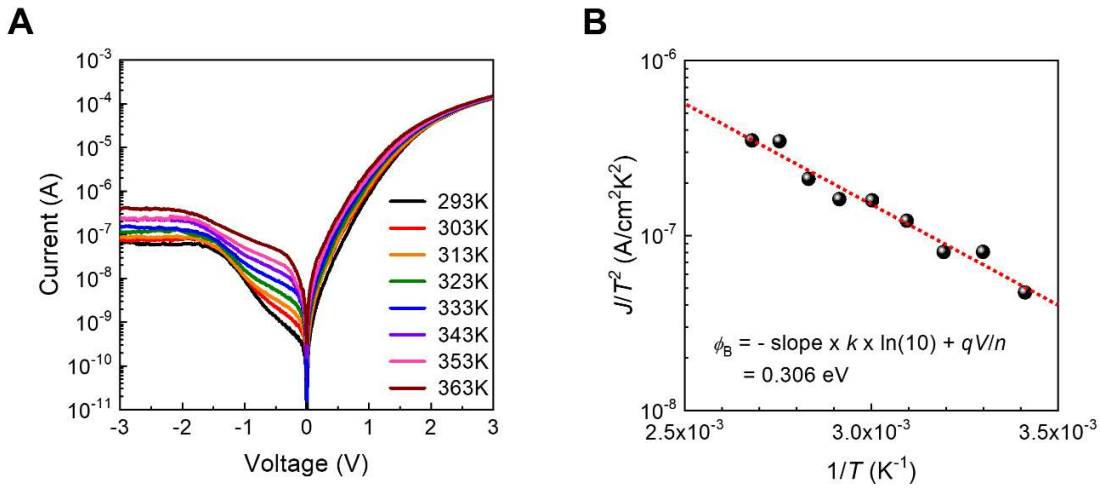

Fig. S13. Temperature-dependent current transport characteristics. (**A**) Temperature-dependent current-voltage (*I-V*) characteristics. (**B**) log(J/T^2) vs $1/T$ plot under forward bias. V=0.1 V and n=1.31 are used to calculate the barrier.

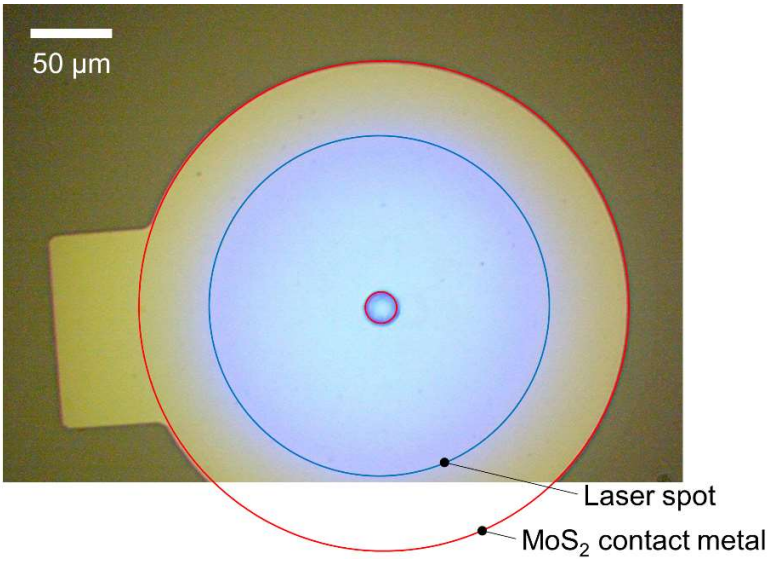

Fig. S14. Laser spot size compared to the MoS_2 contact metal.

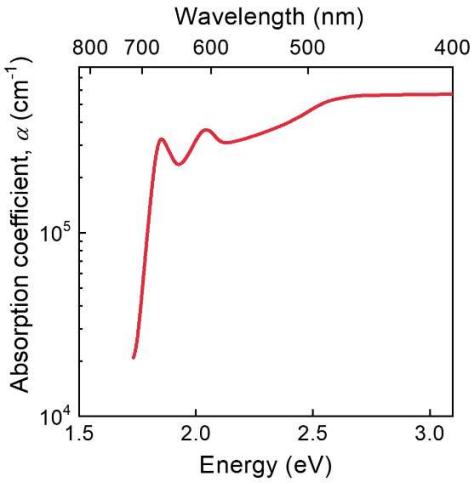

Fig. S15. Measured absorption spectrum of 69-nm MoS_2 flake.

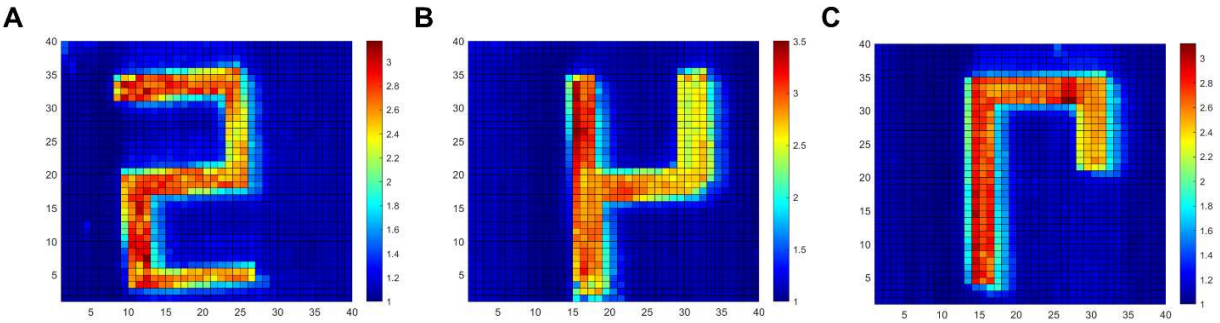

Fig. S16. Infrared imaging capability of the MoS_2/Ge heterostructure. Various geometries are imaged, such as (**A**) "2," (**B**) "4," and (**C**) "7."

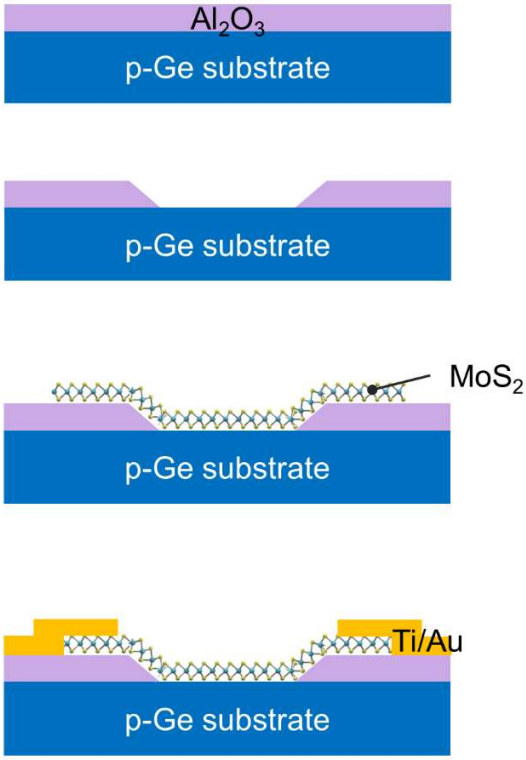

Fig. S17. Schematic of the fabrication of the p-Ge/MoS_2 quasi van der Waals heterojunction photodetector.

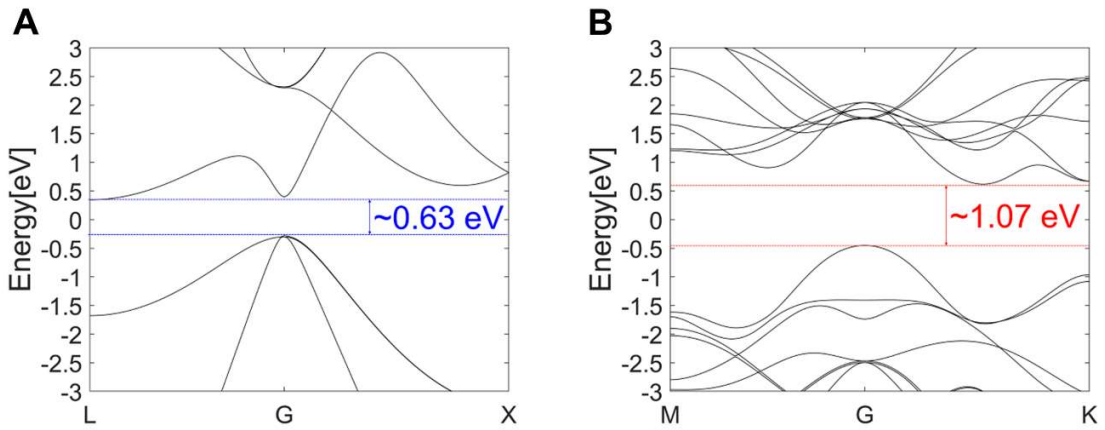

Fig. S18. Band structures of materials in the heterostrucure. Band structure of (**A**) bulk Ge and (**B**) bulk MoS_2.

Dual-band (ref)	Structure	Materials	Responsivity (AW^{-1})	Applications	Year
NIR/VIS (This work)	Heterojunction	p-Ge/MoS_2	<2.5	Selective imaging	-
SWIR/MWIR (12)	Back-to-back	CQDs	$<10^{-2}$	Imaging, temperature recognition	2019
NIR/VIS (14)	Heterojunction	Organics	$>10^{2}$	-	2020
NIR/VIS (15)	Back-to-back	pn-Ge/pn-Si	<0.6	-	2019
UV/MIR (38)	Back-to-back (3-terminal)	ZnO-NN/ G/InAs-NN	<15	-	2021
UV-VIS-NIR (39)	Heterojunction	Perovskite/Si	<0.05	-	2020

Table. S1. Comparison of recent multi-band photodetectors.

REFERENCES AND NOTES

1. J. Ma, C. Chen, C. Li, J. Huang, Infrared and visible image fusion via gradient transfer and total variation minimization. *Inf. Fusion* **31**, 100–109 (2016).

2. J. Ma, W. Yu, P. Liang, C. Li, J. Jiang, FusionGAN: A generative adversarial network for infrared and visible image fusion. *Inf. Fusion* **48**, 11–26 (2019).

3. M. Kamimura, N. Kanayama, K. Tokuzen, K. Soga, Y. Nagasaki, Near-infrared (1550 nm) in vivo bioimaging based on rare-earth doped ceramic nanophosphors modified with PEG-b-poly(4-vinylbenzylphosphonate). *Nanoscale* **3**, 3705–3713 (2011).

4. R. V McDaniel, D. A. Scribner, W. K. Krebs, P. R. Warren, N. Ockman, J. McCarley, in *Infrared Technology and Applications XXIV*, B. F. Andresen, M. Strojnik, Eds. (SPIE, 1998), vol. 3436, pp. 685–695.

5. Y. Zou, L. Zhang, C. Liu, B. Wang, Y. Hu, Q. Chen, in *AI and Optical Data Sciences II* (SPIE, 2021), vol. 11703, p. 62.

6. M. C. Al Naboulsi, H. Sizun, F. de Fornel, Fog attenuation prediction for optical and infrared waves. *Opt. Eng.* **43**, 319–329 (2004).

7. Z. Xia, Z. Z. Wei, Fabrication and performance of a NiMn2O4/LaNiO3 composite film detector with multi electrodes for night vision imaging application. *Sensors Actuators A Phys.*, 112713 (2021).

8. X. Jiang, S. Wilton, I. Kudryashov, M. A. Itzler, M. Entwistle, J. Kotelnikov, A. Katsnelson, B. Piccione, M. Owens, K. Slomkowski, S. Roszko, S. Rangwala, in *Optical Sensing, Imaging, and Photon Counting: From X-Rays to THz*, O. Mitrofanov, C. H. Tan, J. L. P. Vizcaíno, M. Razeghi, Eds. (SPIE, 2018), vol. 10729, pp. 33–44.

9. Y. Cao, J. Zhu, J. Xu, J. He, J.-L. Sun, Y. Wang, Z. Zhao, Ultra-broadband photodetector for the visible to terahertz range by self-assembling reduced graphene oxide-silicon nanowire array heterojunctions. *Small* **10**, 2345–2351 (2014).

10. J. W. Lee, D. Y. Kim, S. Baek, H. Yu, F. So, Inorganic UV–visible–SWIR broadband photodetector based on monodisperse PbS nanocrystals. *Small* **12**, 1328–1333 (2016).

11. W. Hu, H. Cong, W. Huang, Y. Huang, L. Chen, A. Pan, C. Xue, Germanium/perovskite heterostructure for high-performance and broadband photodetector from visible to infrared telecommunication band. *Light Sci. Appl.* **8**, 106 (2019).

12. X. Tang, M. M. Ackerman, M. Chen, P. Guyot-Sionnest, Dual-band infrared imaging using stacked colloidal quantum dot photodiodes. *Nat. Photonics* **13**, 277–282 (2019).

13. Z. Lan, Y. Lei, W. K. E. Chan, S. Chen, D. Luo, F. Zhu, Near-infrared and visible light dual-mode organic photodetectors. *Sci. Adv.* **6**, eaaw8065 (2020).

14. Y. Wang, B. Siegmund, Z. Tang, Z. Ma, J. Kublitski, S. Xing, V. C. Nikolis, S. Ullbrich, Y. Li, J. Benduhn, D. Spoltore, K. Vandewal, K. Leo, Stacked dual-wavelength near-infrared organic photodetectors. *Adv. Opt. Mater.* **9**, 2001784 (2021).

15. E. T. Simola, A. De Iacovo, J. Frigerio, A. Ballabio, A. Fabbri, G. Isella, L. Colace, Voltage-tunable dual-band Ge/Si photodetector operating in VIS and NIR spectral range. *Opt. Express* **27**, 8529–8539 (2019).

16. P. J. Collings, Simple measurement of the band gap in silicon and germanium. *Am. J. Phys.* **48**, 197–199 (1980).

17. K. F. Mak, C. Lee, J. Hone, J. Shan, T. F. Heinz, Atomically ThinMoS2: A new direct-gap semiconductor. *Phys. Rev. Lett.* **105**, 136805 (2010).

18. R. D. Mahyavanshi, G. Kalita, A. Ranade, P. Desai, M. Kondo, T. Dewa, M. Tanemura, Photovoltaic action with broadband photoresponsivity in germanium-MoS2 ultrathin heterojunction. *IEEE Trans. Electron Devices* **65**, 4434–4440 (2018).

19. X. Zhang, F. Lou, C. Li, X. Zhang, N. Jia, T. Yu, J. He, B. Zhang, H. Xia, S. Wang, X. Tao, Flux method growth of bulk MoS2 single crystals and their application as a saturable absorber. *CrystEngComm* **17**, 4026–4032 (2015).

20. M. H. Chiu, C. Zhang, H. W. Shiu, C. P. Chuu, C. H. Chen, C. Y. S. Chang, C. H. Chen, M. Y. Chou, C. K. Shih, L. J. Li, Determination of band alignment in the single-layer MoS_2/WSe_2 heterojunction. *Nat. Commun.* **6**, 7666 (2015).

21. L. Hu, J. Yang, J. Wang, P. Cheng, L. O. Chua, F. Zhuge, All-optically controlled memristor for optoelectronic neuromorphic computing. *Adv. Funct. Mater.* **31**, 2005582 (2021).

22. D. Periyanagounder, P. Gnanasekar, P. Varadhan, J.-H. He, J. Kulandaivel, High performance, self-powered photodetectors based on a graphene/silicon Schottky junction diode. *J. Mater. Chem. C* **6**, 9545–9551 (2018).

23. E. Lachat, H. Macher, T. Landes, P. Grussenmeyer, Assessment and calibration of a RGB-D camera (Kinect v2 Sensor) towards a potential use for close-range 3D modeling. *Remote Sens.* **7**, 13070–13097 (2015).

24. B. Cui, X. Ma, X. Xie, G. Ren, Y. Ma, Classification of visible and infrared hyperspectral images based on image segmentation and edge-preserving filtering. *Infrared Phys. Technol.* **81**, 79–88 (2017).

25. S. Manzeli, D. Ovchinnikov, D. Pasquier, O. V. Yazyev, A. Kis, 2D transition metal dichalcogenides. *Nat. Rev. Mater.* **2**, 17033 (2017).

26. S. Goossens, G. Navickaite, C. Monasterio, S. Gupta, J. J. Piqueras, R. Pérez, G. Burwell, I. Nikitskiy, T. Lasanta, T. Galán, E. Puma, A. Centeno, A. Pesquera, A. Zurutuza, G. Konstantatos, F. Koppens, Broadband image sensor array based on graphene–CMOS integration. *Nat. Photonics* **11**, 366–371 (2017).

27. T. Mueller, E. Malic, Exciton physics and device application of two-dimensional transition metal dichalcogenide semiconductors. *npj 2D Mater. Appl.* **2**, 29 (2018).

28. D. Y. Song, D. Chu, S. K. Lee, S. W. Pak, E. K. Kim, High photoresponsivity from multilayer MoS2/Si heterojunction diodes formed by vertically stacking. *J. Appl. Phys.* **122**, 124505 (2017).

29. P. L. Richards, Bolometers for infrared and millimeter waves. *J. Appl. Phys.* **76**, 1–24 (1994).

30. J. Taylor, H. Guo, J. Wang, Ab initio modeling of quantum transport properties of molecular electronic devices. *Phys. Rev. B* **63**, 245407 (2001).

31. M. Brandbyge, J.-L. Mozos, P. Ordejón, J. Taylor, K. Stokbro, Density-functional method for nonequilibrium electron transport. *Phys. Rev. B* **65**, 165401 (2002).

32. O. M. Nayfeh, C. N. Chleirigh, J. Hennessy, L. Gomez, J. L. Hoyt, D. A. Antoniadis, Design of tunneling field-effect transistors using strained-silicon/strained-germanium type-II staggered heterojunctions. *IEEE Electron Device Lett.* **29**, 1074–1077 (2008).

33. K. F. Longenbach, R. Beresford, W. I. Wang, A complementary heterostructure field effect transistor technology based on InAs/AlSb/GaSb. *IEEE Trans. Electron Devices* **37**, 2265–2267 (1990).

34. K. Bhatnagar, M. P. Caro, J. S. Rojas-Ramirez, R. Droopad, P. M. Thomas, A. Gaur, M. J. Filmer, S. L. Rommel, Integration of broken-gap heterojunction InAs/GaSb Esaki tunnel diodes on silicon. *J. Vac. Sci. Technol. B* **33**, 62203 (2015).

35. K.-S. Hsu, W.-C. Hung, C.-C. Chang, W.-H. Lin, M.-H. Shih, P.-T. Lee, S.-Y. Lin, S.-W. Chang, Y.-C. Chang, Lasing action and extraordinary reduction in long radiative lifetime of type-II GaSb/GaAs quantum dots using circular photonic crystal nanocavity. *Appl. Phys. Lett.* **107**, 091113 (2015).

36. H.-T. Lin, K.-S. Hsu, C.-C. Chang, W.-H. Lin, S.-Y. Lin, S.-W. Chang, Y.-C. Chang, M.-H. Shih, Photonic crystal circular nanobeam cavity laser with type-II GaSb/GaAs quantum rings as gain material. *Sci. Rep.* **10**, 4757 (2020).

37. M.-H. Doan, Y. Jin, S. Adhikari, S. Lee, J. Zhao, S. C. Lim, Y. H. Lee, Charge transport in MoS2/WSe2 van der Waals heterostructure with tunable inversion layer. *ACS Nano* **11**, 3832–3840 (2017).

38. Y. Tchoe, J. Jo, H. Kim, H. Kim, H. Baek, K. Lee, D. Yoo, W. J. Choi, M. Kim, G.-C. Yi, Vertical monolithic integration of wide- and narrow-bandgap semiconductor nanostructures on graphene films. *NPG Asia Mater.* **13**, 33 (2021).

39. W. Qu, S. Weng, L. Zhang, M. Sun, B. Liu, W. Du, Y. Zhang, Self-powered ultraviolet–visible–near infrared perovskite/silicon hybrid photodetectors based on a novel Si/SnO2/MAPbI3/MoO3 heterostructure. *Appl. Phys. Express* **13**, 121001 (2020).